

OPEN

One- and two-dimensional electromagnetically induced gratings in an Er^{3+} - doped yttrium aluminum garnet crystal

Tao Shui¹, Ling Li², Xin Wang² & Wen-Xing Yang^{1*}

A coherently prepared Er^{3+} -doped yttrium aluminum garnet (YAG) crystal with a four-level ionic configuration is exploited for realizing one-dimensional (1D) and two-dimensional (2D) electromagnetically induced gratings (EIGs). Owing to the probe gain induced by the incoherent pump, the diffraction efficiency of the crystal grating, especially the first-order diffraction, can be significantly improved via increasing the incoherent pumping rate or decreasing the probe detuning. The enhancement of the grating diffraction efficiency originates from the interference between the gain and phase gratings. It is also demonstrated that the diffraction of the crystal grating can be dynamically controlled via tuning the intensity and detuning of the standing-wave driving field or the concentration of Er^{3+} ion. More importantly, the probe energy of the diffraction side lobes around the central principle maximum is comparable to that of the first-order diffraction field for small driving intensity or large driving detuning. Our scheme may provide a possibility for the active all-optical control of optical switching, routing and storage in fiber communication wavelengths.

In the past few decades, the study of electromagnetically induced grating (EIG) has been one of the hot spots in optics due to its potential applications in optical switching and routing^{1,2}, optical bistability³, light storage⁴, self-imaging^{5,6}, and four-wave mixing dipole soliton⁷. Note that EIG, which is created by using a standing-wave (SW) laser field to replace the traveling-wave laser field in electromagnetically induced transparency, can diffract the incident probe beam into high-order diffraction directions. Such a diffraction grating is derived from the spatial periodic modulation of the amplitude and phase of the transmission function. It was first theoretically proposed by Xiao *et al.*⁸ and experimentally observed in cold atomic systems^{9,10}. Since then, EIG has been extensively investigated in atomic systems^{11–22}, crystal of molecular magnets system²³, quantum wells and dots^{24–27} and hybrid artificial molecule^{28,29}. Among these studies, the improvement of the diffraction efficiency of the coherent grating can be achieved via some feasible approaches such as giant Kerr nonlinearity¹¹, Raman gain¹⁴, parity-time symmetry (or antisymmetry)^{18–20,26}, van der Waals interaction²² and the surface plasmon and tunneling effect²⁹.

On the other hand, much attention has been attracted to the study of Er^{3+} -doped yttrium-aluminum-garnet (YAG, chemical formula $\text{Y}_3\text{Al}_5\text{O}_{12}$) crystal since the stimulated emission from Er^{3+} ions in the YAG crystal was first observed by Zharikov *et al.*³⁰. It should be worth pointing out that Er^{3+} -doped YAG crystal, where some of the Y^{3+} ions are replaced by Er^{3+} ions, is an efficient active medium for solid-state lasers operating in the eye-safe wavelengths³¹, which have been applied to the fields of optical communication and biomedicine. Recent years, based on the atomic coherence and quantum interference effects, many kinds of quantum optical phenomena, such as electromagnetically induced transparency (EIT)³², large refractive index with vanishing absorption³³, positive and negative dispersion³⁴, flattened gain³⁵ and optical bistability and multistability^{36,37}, have been studied in Er^{3+} -doped YAG crystals. These solid-state systems based on the Er^{3+} -doped YAG crystals have the similar properties to atomic vapors, but with the advantage of no atomic diffusion. So far, to our best knowledge, studies have not been extended to the investigation of the diffraction of the EIG in the Er^{3+} -doped YAG crystal.

In this paper, we investigate the Fraunhofer diffraction characteristics of one-dimensional (1D) and two-dimensional (2D) diffraction gratings realized in an Er^{3+} -doped YAG crystal with four-level ionic configuration. By taking advantage of the incoherent pumping process and the periodic spatial modulation of the driving

¹School of Physics and Optoelectronic Engineering, Yangtze University, Jingzhou, Hubei, 434023, China.

²Department of Physics, Southeast University, Nanjing, 211189, China. *email: wenxingyang2@126.com

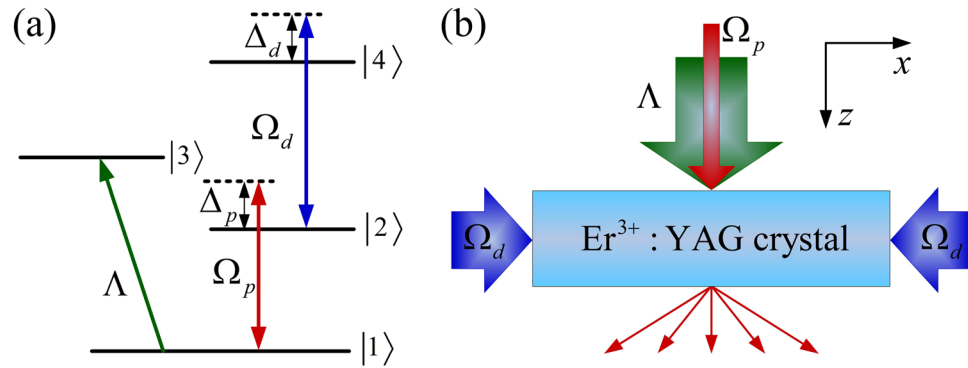


Figure 1. (a) Schematic of diagram of a four-level Er^{3+} ionic system interacting with probe, driving and incoherent pumping fields. (b) Sketch of the spatial configuration of the three laser beams with respect to the crystal and diffraction orders.

field with standing wave pattern, a gain grating or hybrid (gain-phase) grating with high diffraction efficiency can be realized. We demonstrate that the incoherent pumping field and the probe detuning play important roles on the forming of the 1D and 2D gratings and their diffraction efficiency. By increasing the incoherent pumping rate and decreasing the probe detuning, we can significantly enhance the interference between the gain and phase gratings, and thereby improving the diffraction efficiency of the crystal grating. Furthermore, it is found that the diffraction efficiency of the crystal gratings is controllable by tuning the probe detuning and the intensity and detuning of the SW driving field or the concentration of Er^{3+} ion. More importantly, the probe energy of the diffraction side lobes around the zeroth diffraction order is comparable to that of the first-order diffraction for small driving intensity or large driving detuning. Moreover, our results also show that 1D and 2D crystal gratings exhibit different diffraction characteristics for the same optical parameters. Such crystal gratings, operating in the fiber communication band, may be more useful in optical communication and optical information processing.

Model and Method

Light-matter interactions in Er^{3+} -doped YAG crystal. As schematically shown in Fig. 1(a), we consider a four-level Er^{3+} ionic system in an Er^{3+} -doped YAG crystal. The designated states can be chosen as follows: $|1\rangle = {}^4I_{15/2}$, $|2\rangle = {}^4I_{13/2}$, $|3\rangle = {}^4I_{11/2}$ and $|4\rangle = {}^4I_{9/2}$. A weak probe field E_p with Rabi frequency Ω_p and an incoherent pumping field with a pumping rate R are applied to the transitions $|2\rangle \rightarrow |1\rangle$ and $|3\rangle \rightarrow |1\rangle$, respectively, while the transition $|4\rangle \rightarrow |2\rangle$ is driven by a strong driving field E_d with Rabi frequency Ω_d . Here, we take the level $|1\rangle$ as the energy origin. In the Schrödinger picture and under the electric-dipole and rotating-wave approximations, the total Hamiltonian for the four-level Er^{3+} ionic system is given by

$$H = \hbar\omega_{21} |2\rangle\langle 2| + \hbar(\omega_{32} + \omega_{21})|3\rangle\langle 3| + \hbar(\omega_{42} + \omega_{21})|4\rangle\langle 4| - \hbar(\Omega_p e^{-i\omega_p t} |2\rangle\langle 1| + \Omega_d e^{-i\omega_d t} |4\rangle\langle 2| + H.c.), \tag{1}$$

where ω_{ij} is the corresponding resonance frequency of the transition $|i\rangle \rightarrow |j\rangle$. We choose $H_0 = \hbar\omega_{21} |2\rangle\langle 2| + \hbar(\omega_{32} + \omega_{21})|4\rangle\langle 4|$ as the free Hamiltonian. Using the transform formula $H_I = e^{iH_0 t/\hbar}(H - H_0)e^{-iH_0 t/\hbar}$, we obtain the interaction Hamiltonian in the interaction picture, which is written as

$$H_I = -\hbar\Delta_p |2\rangle\langle 2| - \hbar(\Delta_p + \Delta_c)|4\rangle\langle 4| - \hbar(\Omega_p |2\rangle\langle 1| + \Omega_d |4\rangle\langle 2| + H.c.), \tag{2}$$

where $\Delta_p = \omega_p - \omega_{21}$ and $\Delta_d = \omega_d - \omega_{42}$ are the detunings of the probe and driving fields, respectively. Equation (2) describes the interaction between the coherent applied fields and Er^{3+} ions. It is worth noting that Eq. (2) can also be rewritten in a 4×4 matrix form:

$$H_I = -\hbar \begin{pmatrix} 0 & \Omega_p^* & 0 & 0 \\ \Omega_p & \Delta_p & 0 & \Omega_d^* \\ 0 & 0 & 0 & 0 \\ 0 & \Omega_d & 0 & \Delta_p + \Delta_d \end{pmatrix}. \tag{3}$$

The dynamics of the atomic system can be described by using the density matrix approach as

$$\frac{\partial \rho}{\partial t} = -\frac{i}{\hbar}[H_I, \rho] + L[\rho(t)]. \tag{4}$$

Here, the Liouvillian matrix $L[\rho(t)]$ indicating the irreversible relaxation can be written as

$$L[\rho(t)] = \begin{pmatrix} \sigma_{11} & -\gamma_{21}\rho_{12} & -\gamma_{31}\rho_{13} & -\gamma_{41}\rho_{14} \\ -\gamma_{21}\rho_{21} & \sigma_{22} & -\gamma_{32}\rho_{23} & -\gamma_{42}\rho_{24} \\ -\gamma_{31}\rho_{31} & -\gamma_{32}\rho_{32} & -\sigma_{33} & -\gamma_{43}\rho_{34} \\ -\gamma_{41}\rho_{41} & -\gamma_{42}\rho_{42} & -\gamma_{43}\rho_{43} & -\sigma_{44} \end{pmatrix}, \tag{5}$$

where $\sigma_{11} = R(\rho_{33} - \rho_{11}) + \Gamma_{21}\rho_{22} + \Gamma_{31}\rho_{33} + \Gamma_{41}\rho_{44}$, $\sigma_{22} = \Gamma_{32}\rho_{33} + \Gamma_{42}\rho_{44} - \Gamma_{21}\rho_{22}$, $\sigma_{33} = R(\rho_{33} - \rho_{11}) + (\Gamma_{31} + \Gamma_{32})\rho_{33} - \Gamma_{43}\rho_{44}$ and $\sigma_{44} = (\Gamma_{41} + \Gamma_{42} + \Gamma_{43})\rho_{44}$. Γ_{ij} is the spontaneous-emission decay rate from the state $|i\rangle$ to the state $|j\rangle$, while γ_{ij} is the decay rate of the coherence between the states $|i\rangle$ and $|j\rangle$ ($i, j = 1, 2, 3, 4; i > j$), given by $\gamma_{21} = (\Gamma_{21} + R + \gamma_{21}^{dph})/2$, $\gamma_{31} = (\Gamma_{31} + \Gamma_{32} + 2R + \gamma_{31}^{dph})/2$, $\gamma_{32} = (\Gamma_{31} + \Gamma_{32} + \Gamma_{21} + R + \gamma_{32}^{dph})/2$, $\gamma_{41} = (\Gamma_{41} + \Gamma_{42} + \Gamma_{43} + R + \gamma_{41}^{dph})/2$, $\gamma_{42} = (\Gamma_{41} + \Gamma_{42} + \Gamma_{43} + \Gamma_{21} + \gamma_{42}^{dph})/2$ and $\gamma_{43} = (\Gamma_{41} + \Gamma_{42} + \Gamma_{43} + \Gamma_{31} + \Gamma_{31} + R + \gamma_{43}^{dph})/2$. The Rabi frequencies of the probe and driving fields are defined by

$$\Omega_p = \mu_{21}E_p/2\hbar, \Omega_d = \mu_{42}E_d/2\hbar, \tag{6}$$

where μ_{ij} is the electric-dipole matrix moment between level $|i\rangle$ and level $|j\rangle$, which can be calculated via the following equation^{38,39}:

$$\begin{aligned} \mu_{ij}^2 &= |\langle \psi | er | \psi \rangle|^2 \\ &= \frac{2}{2J + 1} \frac{2}{2J' + 1} e^2 \sum_{m=2,4,6} \Omega_m |\langle 4f^N(\alpha SL)J || U^m || 4f^N(\alpha' S' L')J' \rangle|^2, \end{aligned} \tag{7}$$

where Ω_m ($m = 2, 4, 6$) represents the phenomenological intensity parameter, J and J' are the quantum numbers of angular momentum of the state $|i\rangle$ and $|j\rangle$, respectively. The factor 2 in Eq. (7) arose from the Kramers degenerate of the Stark levels of the Er^{3+} ion. The squared reduced matrix element $|\langle 4f^N(\alpha SL)J || U^m || 4f^N(\alpha' S' L')J' \rangle|^2$ can be obtained⁴⁰ and the spectral intensity parameters can be described by an empirical formula⁴¹

$$\Omega_m(10^{-20}) = 1.25X^{1/4} \exp[-0.4(X - A)^{2/3}] + B, \tag{8}$$

where X is the concentration of the doped Er^{3+} ions. A and B are empirical parameters: $A = 1.0$ and $B = 0.33$ for Ω_2 ; $A = 1.1$ and $B = 0.7$ for Ω_4 ; $A = 1.4$ and $B = 0.59$ for Ω_6 .

In the limit of weak probe field, a perturbation expansion method is used for deriving the analytical and steady-state solution for ρ_{ij}^l ($i, j = 1, 2, 3, 4$). We take the expansions $\rho_{ij} = \sum_{m=0}^{\infty} \varepsilon^m \rho_{ij}^{(m)}$ and $\Omega_p = \sum_{n=1}^{\infty} \varepsilon^n \Omega_p^{(n)}$ and solve Eq. (4) order by order. At the zero order, we obtain non-zero density-matrix elements as

$$\begin{aligned} \rho_{11}^{(0)} &= \frac{\kappa_1\Gamma_{21}\Gamma_{31} + \kappa_1\Gamma_{21}\Gamma_{32} + \kappa_3\Gamma_{31}\Gamma_{41} + \kappa_3\Gamma_{32}\Gamma_{41} + \kappa_3\Gamma_{31}\Gamma_{43}}{\kappa_1\kappa_2 + \kappa_3\kappa_4}, \\ \rho_{22}^{(0)} &= \frac{\kappa_1\Gamma_{32}R}{\kappa_1\kappa_2 + \kappa_3\kappa_4}, \\ \rho_{33}^{(0)} &= \frac{\kappa_1\Gamma_{21}R + \kappa_3\Gamma_{41}R + \kappa_3\Gamma_{42}R}{\kappa_1\kappa_2 + \kappa_3\kappa_4}, \\ \rho_{44}^{(0)} &= \frac{\kappa_3\Gamma_{32}R}{\kappa_1\kappa_2 + \kappa_3\kappa_4}, \end{aligned} \tag{9}$$

where $\kappa_1 = \Gamma_{41} + \Gamma_{42} + \Gamma_{43} + [2|\Omega_d|^2\gamma_{42}/(\gamma_{42}^2 + \Delta_d^2)]$, $\kappa_2 = \Gamma_{21}\Gamma_{31} + \Gamma_{21}\Gamma_{32} + 2\Gamma_{21}R + \Gamma_{32}R$, $\kappa_3 = 2|\Omega_d|^2\gamma_{42}/(\gamma_{42}^2 + \Delta_d^2)$ and $\kappa_4 = \Gamma_{31}\Gamma_{41} + \Gamma_{32}\Gamma_{41} + \Gamma_{31}\Gamma_{43} + \Gamma_{32}R + 2\Gamma_{41}R + 2\Gamma_{43}R$.

At the first order, we obtain

$$\rho_{21}^{(1)} = \frac{i(\rho_{11}^{(0)} - \rho_{22}^{(0)})\Omega_p - \frac{i|\Omega_d|^2(\rho_{44}^{(0)} - \rho_{22}^{(0)})\Omega_p}{[\gamma_{41} - i(\Delta_p + \Delta_d)](\gamma_{42} - i\Delta_d)}}{\gamma_{21} - i\Delta_p + \frac{|\Omega_d|^2}{\gamma_{41} - i(\Delta_p + \Delta_d)}}. \tag{10}$$

Therefore, the probe susceptibility χ_p can be written as

$$\chi_p = \frac{N_0|\mu_{21}|^2}{\epsilon_0\hbar\Omega_p} \rho_{21}^{(1)} = \frac{N_0|\mu_{21}|^2}{\epsilon_0\hbar\Gamma} \chi = \frac{N_0|\mu_{21}|^2}{\epsilon_0\hbar\Gamma} \cdot \frac{i(\rho_{11}^{(0)} - \rho_{22}^{(0)}) - \frac{i|\Omega_d|^2(\rho_{44}^{(0)} - \rho_{22}^{(0)})}{[\gamma_{41} - i(\Delta_p + \Delta_d)](\gamma_{42} - i\Delta_d)}}{\gamma_{21} - i\Delta_p + \frac{|\Omega_d|^2}{\gamma_{41} - i(\Delta_p + \Delta_d)}} \Gamma, \tag{11}$$

where N_0 denotes the number of doped ions per unit volume. Note that the real and imaginary parts of probe susceptibility χ_p represent the dispersion and absorption-gain, respectively.

Fraunhofer diffraction of 1D EIG. It can be seen from Eq. (11) that both the real and imaginary parts of the probe susceptibility χ_p depend on the intensity of the driving field. The space-dependent driving field can

result in the spatial modulation of the dispersion and absorption-gain for probe field. In this case, the Er^{3+} -doped YAG crystal can be treated as an EIG. For 1D EIG, the 1D space-dependent driving field $\Omega_d(x)$ is a SW field, which can be written as

$$\Omega_d(x) = \Omega_{d0} \sin(\pi x/\Lambda), \quad (12)$$

where 2Λ is the spatial period of the SW field. In this situation, 1D EIG can diffract the probe beam propagating in the z direction into different diffraction directions. Under the slowly varying envelope approximation and in the steady-state regime, the propagation of the probe field is described by the reduced wave equation as

$$\frac{\partial E_p}{\partial z} = i \frac{\pi}{\epsilon_0 \lambda_p} P = i \frac{\pi}{\lambda_p} \chi_p E_p, \quad (13)$$

where λ_p is the wavelength of the probe beam. Equation (13) can be rewritten as $\partial E_p / \partial z' = i \chi_p E_p$, where $z' = (\pi N_0 |\mu_{21}|^2) \cdot z / (\epsilon_0 \hbar \lambda_p \Gamma)$. Note that z' is a dimensionless variable by setting $\zeta = (\epsilon_0 \hbar \lambda_p \Gamma) / (\pi N_0 |\mu_{21}|^2)$ as the unit of z .

We assume that the interaction length between Er^{3+} ions and probe field along the z direction, i.e., the thickness of the thin Er^{3+} -doped YAG crystal, is L . Thus, the transmission function, which is defined as the ratio of the output field amplitude to the input field amplitude, can be given by

$$T(x) = e^{-Im[\chi(x)]L} e^{iRe[\chi(x)]L}, \quad (14)$$

where $|T(x)| = e^{-Im[\chi(x)]L}$ and $\Phi(x) = Re[\chi(x)]L$ are the amplitude and phase of 1D transmission function, respectively. Such a grating is the superposition of an amplitude grating and a phase grating.

By 1D Fourier transform of $T(x)$, we can obtain 1D Fraunhofer diffraction-intensity function:

$$I_p(\theta) = |F(\theta)|^2 \frac{\sin^2(M\pi \Lambda \sin\theta/\lambda_p)}{M^2 \sin^2(\pi \Lambda \sin\theta/\lambda_p)}, \quad (15)$$

where θ indicates the diffraction angle with respect to the z direction and M represents the number of spatial periods of the atomic grating illuminated by the probe beam. $F(\theta)$ is the Fraunhofer diffraction of a single space period Λ , which is given by

$$F(\theta) = \frac{1}{\Lambda} \int_0^\Lambda T(x) e^{-i2\pi x \sin\theta/\lambda_p} dx. \quad (16)$$

In particular, if the condition of $\sin\theta_m = m\lambda_p/\Lambda$ is satisfied, the diffraction intensity I_m along the m -order diffraction direction can be calculated by $I_m = |F(\theta_m)|^2 = (1/\Lambda) \int_0^\Lambda T(x) e^{-i2\pi mx/\Lambda} dx$.

Fraunhofer diffraction of 2D EIG. For 2D EIG, the 2D space-dependent driving field $\Omega_d(x', y')$ is a superposition of two orthogonal SW fields with the same frequency along the x and y directions, i.e., $\Omega_d(x', y') = \Omega_{d0} [\sin(\pi x'/\Lambda) + \sin(\pi y'/\Lambda)]$, where $2\Lambda'$ is the period of the two SW fields. It should be noted that xy coordinates are obtained by rotating the xy coordinates counterclockwise 45 degrees, and then $x = \sqrt{2}x'/2 + \sqrt{2}y'/2$ and $y = -\sqrt{2}x'/2 + \sqrt{2}y'/2$. Thus, in the xy coordinates, the 2D driving field can be rewritten as

$$\Omega_d(x, y) = \Omega_{d0} [\sin(\pi(x+y)/\Lambda) + \sin(\pi(-x+y)/\Lambda)], \quad (17)$$

in which $2\Lambda' = \sqrt{2}\Lambda$ is selected. In this case, the dispersion and absorption-gain can be periodically modulated along the x and y directions with the period Λ . Therefore, the 2D transmission function $T(x, y)$ can be written as

$$T(x, y) = e^{-Im[\chi(x,y)]L} e^{iRe[\chi(x,y)]L}, \quad (18)$$

where $|T(x, y)| = e^{-Im[\chi(x,y)]L}$ and $\Phi(x, y) = Re[\chi(x, y)]L$ are the amplitude and phase of the transmission function, respectively.

By 2D Fourier transform of $T(x, y)$, we can obtain 2D Fraunhofer diffraction-intensity function:

$$I_p(\theta_x, \theta_y) = |F(\theta_x, \theta_y)|^2 \frac{\sin^2(M_x \pi \Lambda \sin\theta_x/\lambda_p) \sin^2(M_y \pi \Lambda \sin\theta_y/\lambda_p)}{M_x^2 \sin^2(\pi \Lambda \sin\theta_x/\lambda_p) M_y^2 \sin^2(\pi \Lambda \sin\theta_y/\lambda_p)}, \quad (19)$$

where $\theta_{x(y)}$ indicates the diffraction angle with respect to the z direction in the $x(y) - z$ plane and $M_{x(y)}$ represents the number of spatial periods of the grating along the $x(y)$ direction. The Fraunhofer diffraction $F(\theta_x, \theta_y)$ of a single space period Λ in 2D space is given by

$$F(\theta_x, \theta_y) = \frac{1}{\Lambda^2} \int_0^\Lambda dx e^{-i2\pi x \sin\theta_x/\lambda_p} \int_0^\Lambda dy T(x, y) e^{-i2\pi y \sin\theta_y/\lambda_p}. \quad (20)$$

Here, when both $\sin\theta_x^m = m\lambda_p/\Lambda$ and $\sin\theta_y^n = n\lambda_p/\Lambda$ are satisfied, we can obtain the diffraction intensity $I_{(m,n)}$ along the (m, n) -th-order diffraction direction as $I_{(m,n)} = |F(\theta_x^m, \theta_y^n)|^2 = (1/\Lambda^2) \int_0^\Lambda e^{-i2\pi mx/\Lambda} dx \int_0^\Lambda T(x, y) e^{-i2\pi ny/\Lambda} dy$.

Experimental realization

For the experimental realization, we would like to mention some points of the Er^{3+} -doped YAG crystal for the present study, which are given as follows:

- (I) Based on the experimental results^{41,42}, we can get the spontaneous-emission decay rate Γ_{ij} of the Er^{3+} ions for different concentrations of Er^{3+} ion at room temperature. For simplicity, all the parameters have been scaled by $\Gamma = 239.1\text{s}^{-1}$. So it is reasonable that we choose the parameters as $\Gamma_{21} = \Gamma$, $\Gamma_{31} = 0.8\Gamma$, $\Gamma_{32} = 10\Gamma$, $\Gamma_{41} = 0.86\Gamma$, $\Gamma_{42} = 0.29\Gamma$, $\Gamma_{43} = 0.04\Gamma$ for 0.52 at. % Er^{3+} ion and $\Gamma_{21} = 1.08\Gamma$, $\Gamma_{31} = 0.91\Gamma$, $\Gamma_{32} = 9.89\Gamma$, $\Gamma_{41} = 0.88\Gamma$, $\Gamma_{42} = 0.32\Gamma$, $\Gamma_{43} = 0.07\Gamma$ for 0.79 at. % Er^{3+} .
- (II) According to the experimental result⁴³, we have found that the dephasing time of Er^{3+} -doped YAG crystal with an Er^{3+} concentration of 0.1%, $T_2 = 75 \mu\text{s}$ on the transition $^4I_{15/2} \rightarrow ^4I_{13/2}$ of Er^{3+} at 1526.97 nm, the homogeneous linewidth $\Gamma_h = 4286 \text{ Hz}$. Thus, it is reasonable for us to estimate the dephasing decay rate as $\gamma_{21}^{dph} = \gamma_{31}^{dph} = \gamma_{32}^{dph} = \gamma_{41}^{dph} = \gamma_{42}^{dph} = \gamma_{43}^{dph} = 15\Gamma$.
- (III) Based on Eqs. (7) and (8), we obtain $\mu_{42} = 2.662 \times 10^{-32} \text{ Cm}$ for 0.52 at. % Er^{3+} ion and $\mu_{42} = 2.799 \times 10^{-32} \text{ Cm}$ for 0.79 at. % Er^{3+} ion.

Results and Discussions

In this section, we focus on analyzing the Fraunhofer diffraction characteristics of the probe beam by adjusting the controllable optical parameters of 1D and 2D EIGs realized in an Er^{3+} -doped YAG crystal. Before presenting the numerical results, we first give the credible evaluation of the numerical computation. Our numerical calculation is based on MATLAB R2015b software. We use the embedded FFT package to make 1D and 2D fast Fourier transform of the transmission function $T(x)$ and select $\Lambda/40$ as the step size of Fourier transform. Continuing to increase the sample points and decrease the step size would not result in the change of the diffraction spectra, which can prove the validity of our numerical computation.

For the case of 1D EIG, we first examine in Fig. 2 the influence of incoherent pumping rate R and probe detuning Δ_p on the Fraunhofer diffraction of the crystal grating. Here, we select Er^{3+} : YAG crystal containing 0.52 at. % concentrations of Er^{3+} ion. Typical curves of the amplitude $|T(x)|$ of the transmission function are shown in Fig. 2(a₁–a₃) for various R and Δ_p . It is obvious that the maxima of the amplitude $|T(x)|$ are always located at the nodes of the SW driving field $\Omega_d(x)$. The corresponding curves of the phase $\Phi(x)$ of the transmission function are also plotted in Fig. 2(b₁–b₃). When $\Delta_p = 0$, the amplitude $|T(x)|$ is greatly improved with the increase of R from 1.77Γ to 2.17Γ because of the enhancement of probe gain in the incoherent pump process [see Fig. 2(a₁)], while the phase $\Phi(x)$, which is unaffected by the change of R , always equals to zero due to the zero dispersion in the resonant light-matter interaction [see Fig. 2(b₁)]. That is to say, only amplitude modulation takes place and the crystal grating is a pure gain grating. As shown in Fig. 2(c₁), the diffraction intensities in all diffraction orders are remarkably improved via increasing the incoherent pumping rate, but the central principle maximum (zeroth-order diffraction) always dominates due to the limitation of amplitude grating⁸. As Δ_p is increased from 0 to 8Γ , the space-dependent dispersion exists and the phase $\Phi(x)$ presents an inhomogeneous distribution over one space period. In this case, the crystal grating becomes a hybrid grating. As shown in Fig. 2(a₂, b₂), both the amplitude $|T(x)|$ and the phase modulation depth $\Delta\Phi$, i.e., $\Delta\Phi = \max[\Phi(x)] - \min[\Phi(x)]$, increase with the increase of R from 2.52Γ to 3.32Γ . As we know, the increase of the amplitude modulation can enhance the intensities of the diffraction fields, while the increase of the phase modulation can improve the ratio of the diffraction intensities in the high diffraction directions. In this case, the hybrid grating can be treated as a superposition of a gain grating and a phase grating¹⁹, increasing the amplitude and phase modulations can enhance the interference between the gain and phase gratings, and thereby leading to the improvement of the diffraction efficiencies and more probe energy being diffracted into high diffraction orders. It is worth noting that the hybrid grating requires stronger incoherent pumping rate than the pure gain grating under the condition of achieving the same first-order diffraction intensity [see red dotted lines in Fig. 2(c₁, c₂)]. For a fixed incoherent pumping rate, i.e., $R = 3.32\Gamma$, when the probe detuning Δ_p is varied from 7Γ to 9Γ , the amplitude $|T(x)|$ is decreased but the phase $\Phi(x)$ with $\Delta\Phi \simeq \pi$ remains almost unchanged [see Fig. 2(a₃, b₃)]. The decrease of the amplitude modulation weakens the interference of the gain and phase gratings. Thus, the diffraction intensities of the diffraction fields decrease. However, the first-order diffraction peak is always highest owing to unchanged phase modulation [see Fig. 2(c₃)]. In order to gain overall view of the effect of the incoherent pumping rate R and probe detuning Δ_p , we present the corresponding evolutions of the diffraction spectra $I_p(\theta)$ with the increase of R and Δ_p in Fig. 3, respectively. It is found that the diffraction efficiency of the crystal grating increases monotonically as R increases in the range of $[2\Gamma, 3.5\Gamma]$ or Δ_p decreases in the range of $[7\Gamma, 11\Gamma]$ [see Fig. 3(a,b)].

To obtain the corresponding power of the incoherent pumping field, the incoherent pumping rate R can be written as $R = \sigma_{13} I_{ip} / h\nu_{ip}$, where ν_{ip} and I_{ip} are the frequency and light intensity of the incoherent pumping field, respectively. h is Planck constant and σ_{13} is the pump absorption section of Er^{3+} ion. The absorption cross-section at 967 nm pump wavelength ($\nu_{ip} = 3.1 \times 10^{14} \text{ s}^{-1}$) is $2.8 \times 10^{-20} \text{ cm}^2$ ^{44,45}. Thus, the light intensity I_{ip} of the incoherent pumping field can be calculated for a certain value of R . Then, we can obtain the power of the incoherent pumping field via the formula $P = AI_{ip}$, where A is the cross-sectional area of the incoherent pumping field. If the laser beam is focused into a spot with a diameter 0.1 mm, this requires the laser power of the incoherent pumping field arrives at $P = 348 \text{ mW}$ for $R = 2.52\Gamma$ and $P = 403 \text{ mW}$ for $R = 2.92\Gamma$. It is obvious that the incoherent

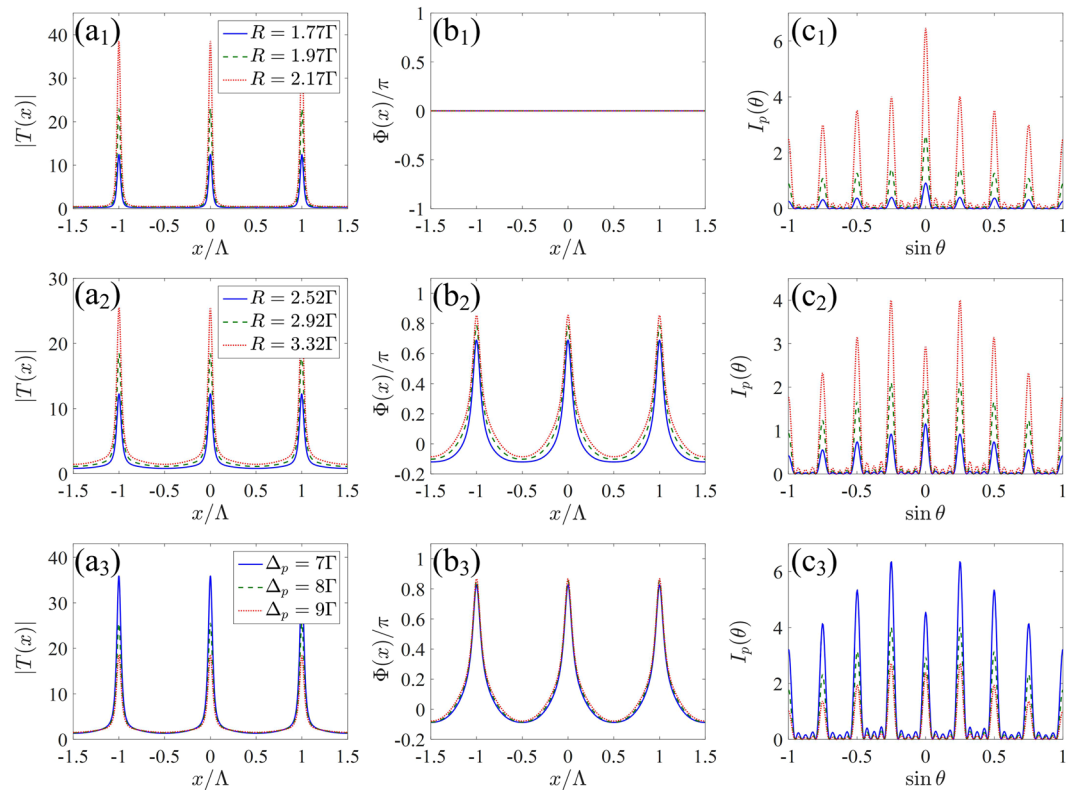


Figure 2. (a₁–a₃) The amplitude $|T(x)|$ and (b₁–b₃) the phase $\Phi(x)/\pi$ of the transmission function as a function of x , and (c₁–c₃) Fraunhofer diffraction intensity $I_p(\theta)$ as a function of $\sin \theta$ for various R and Δ_p . (a₁, b₁, c₁) $\Delta_p = 0$; (a₂, b₂, c₂) $\Delta_p = 8\Gamma$; (a₃, b₃, c₃) $R = 3.32\Gamma$. Other parameters are $\Omega_{d0} = 10\Gamma$, $\Delta_d = 0$, $M = 5$, $\Lambda/\lambda_p = 4$ and $L = 140\zeta$.

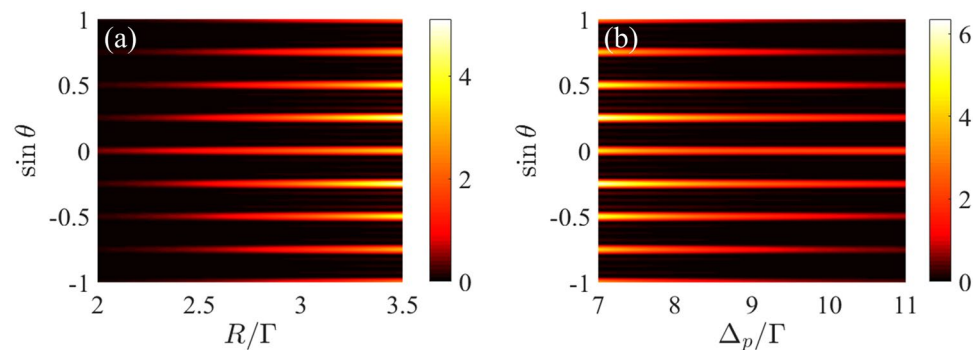


Figure 3. Fraunhofer diffraction spectra of 1D grating as a function of (a) the incoherent pumping rate R with $\Delta_p = 8\Gamma$ and (b) the probe detuning Δ_p with $R = 3.32\Gamma$. Other parameters are the same as in Fig. 2.

pumping field has surpassed the threshold power of the Er^{3+} -doped YAG crystal. In addition, we assume that the incident probe field is sufficiently weak and the interaction length is relatively short. Therefore, our scheme satisfies small-signal model without considering the saturation effect. As for the SW driving field, the selected Rabi frequency, i.e., $\Omega_{d0} = 10\Gamma$, is slightly larger than the selected incoherent pumping rate R . One can readily evaluate that the power of the SW driving field is higher the power of the incoherent pumping field.

We then examine in Fig. 4 how the diffraction distribution of the crystal grating depends on the intensity and detuning of the SW driving field. In Fig. 4(a,b), the extremely large zeroth-order diffraction peaks are truncated and the corresponding intensity of the truncated zeroth-order diffraction field is shown as insets to clearly demonstrate the progress for various Ω_{d0} and Δ_d . Figure 4(a) shows the effect of the intensity Ω_{d0} on Fraunhofer diffraction patterns. With the increase of Ω_{d0} , the zeroth-order diffraction field decreases monotonically, while the diffraction fields in the high-order directions increase firstly and then decrease. In other words, there are optimal values of Ω_{d0} for which the high-order diffraction intensities reach their maxima. In Fig. 4(b), the effect

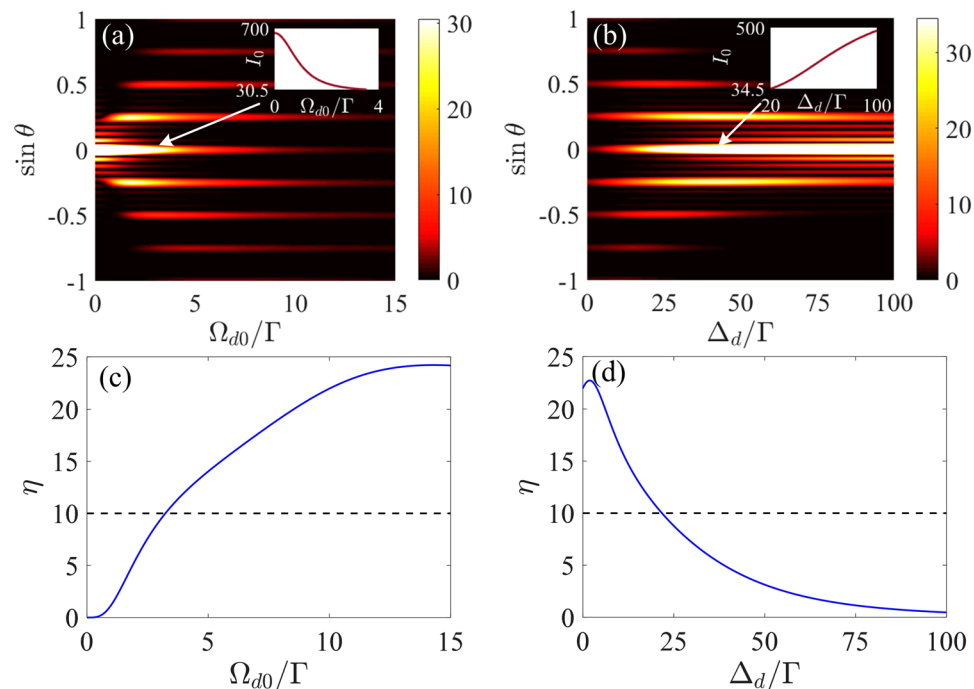


Figure 4. (a,b) Fraunhofer diffraction spectra and (c,d) diffraction contrast η of 1D grating as a function of (a,c) the intensity Ω_{d0} with $\Delta_d = 0$ and (b,d) the detuning Δ_d with $\Omega_{d0} = 10\Gamma$ of the SW driving field. The insets in (a,b) show the diffraction intensity of the truncated zeroth-order diffraction field versus Ω_{d0} and Δ_d , respectively. Other parameters are the same as in Fig. 2 except for $R = 3.32\Gamma$ and $\Delta_p = 8\Gamma$.

of the detuning Δ_d on the diffraction patterns is presented. It can be seen that the high-order diffraction fields also increase firstly and then decrease as Δ_d increases, which is similar to the result in Fig. 4(a), while the diffraction intensity in the central principle maximum increases monotonically. Therefore, one can control the diffraction of the crystal grating by varying the intensity and detuning of the SW driving field. Direct comparison of Fig. 4(a,b) implies that the diffraction side lobes around the zeroth-order diffraction peak have the same evolution trend with the zeroth-order diffraction intensity. More importantly, the probe energy of the diffraction side lobes is comparable to that of the first-order diffraction for small driving intensity or large driving detuning, which would hamper the application of the first-order diffraction component. To choose the suitable parameters to realize the high diffraction efficiency of the first-order diffraction with suppressed diffraction side lobes, we define a “diffraction contrast η ”, which is the intensity ratio of the first-order diffraction to the diffraction side lobe around the central principle maximum, i.e., $\eta = I_1/I_s$. The high performance grating can be obtained when the diffraction contrast η exceeds 10 (i.e., $\eta \geq 10$). It is obvious that the diffraction contrast $\eta \geq 10$ when $\Omega_{d0} \geq 3.24\Gamma$ [see Fig. 4(c)] or $\Delta_d \leq 21.7\Gamma$ [see Fig. 4(d)]. From Fig. 4(a,b), we can find that, in the high performance region, the intensity of the first-order diffraction field reaches its maximal value, i.e., $I_1 = 21.32$ at $\Omega_{d0} = 3.24\Gamma$ and $I_1 = 22.85$ at $\Delta_d = 21.7\Gamma$. In this situation, $\Omega_{d0} = 3.24\Gamma$ and $\Delta_d = 21.7\Gamma$ are the corresponding optimal parameters to realize the optimal performance of the crystal grating.

It has been found that the concentration of Er^{3+} ion can greatly influence the optical properties of Er^{3+} -doped YAG crystal^{32,37}. In the following, we investigate the effect of the concentration of Er^{3+} ion on the diffraction characteristics of the crystal grating in Fig. 5. The concentration of Er^{3+} ion in Er^{3+} -doped YAG crystal greatly affects the electric dipole moment μ_{ij} . We keep the intensity E_{d0} of the standing-wave driving field constant. When $\Omega_{d0} = 10\Gamma$ for 0.52 at. % Er^{3+} ion concentration, we can obtain $\Omega_{d0} = 10.51\Gamma$ for 0.79 at. % Er^{3+} ion concentration. As shown in Fig. 5(a,b), both the amplitude $|T(x)|$ and the phase modulation depth $\Delta\Phi$ decrease with the increase of the Er^{3+} ion concentration from 0.52% to 0.79%. The decrease of both the amplitude and phase modulation reduces the interference between the gain and phase gratings. As a result, the diffraction efficiency of the grating is decreased and the diffraction energy is concentrated into the central principle maximum [see Fig. 5(c)]. These results offer us another controllable parameter to manipulate the diffraction behaviors of the crystal grating.

Let us now investigate the diffraction characteristics of 2D EIG. We also select Er^{3+} : YAG crystal containing 0.52 at. % concentrations of Er^{3+} ion. Such a grating can be realized when the space-dependent driving field is a superposition of two orthogonal SW fields [see Eq. (17)]. Similar to the diffraction of 1D grating, the incoherent pumping rate R and probe detuning Δ_p also play important roles in the energy distribution of different diffraction orders in 2D crystal grating. Figure 6 shows the influence of R and Δ_p on the transmission function and Fraunhofer diffraction patterns of the 2D grating. In the case of $R = 1.833\Gamma$ and $\Delta_p = 0$, the maxima of the amplitude $|T(x, y)|$ are localized at the position (x, y) , where $x = (0.5 \pm m) \cdot \Lambda$ and $y = \pm n \cdot \Lambda$ (m, n are integers), but the phase $\Phi(x, y)$ is zero [see Fig. 6(a₁, b₁)]. In this situation, the grating is a 2D pure gain grating. It can be seen

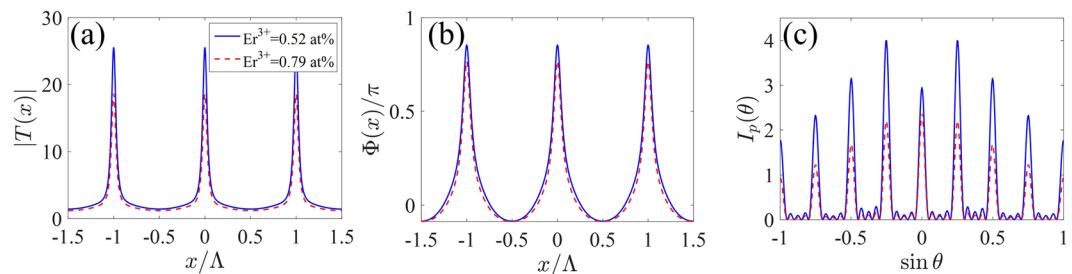


Figure 5. (a) The amplitude $|T(x)|$ and (b) the phase $\Phi(x)/\pi$ of the transmission function as a function of x , and (c) Fraunhofer diffraction intensity $I_p(\theta)$ as a function of $\sin \theta$ for different concentrations of Er^{3+} ion. Other parameters are $R = 3.32\Gamma$, $\Delta_d = 0$ and $\Delta_p = 8\Gamma$.

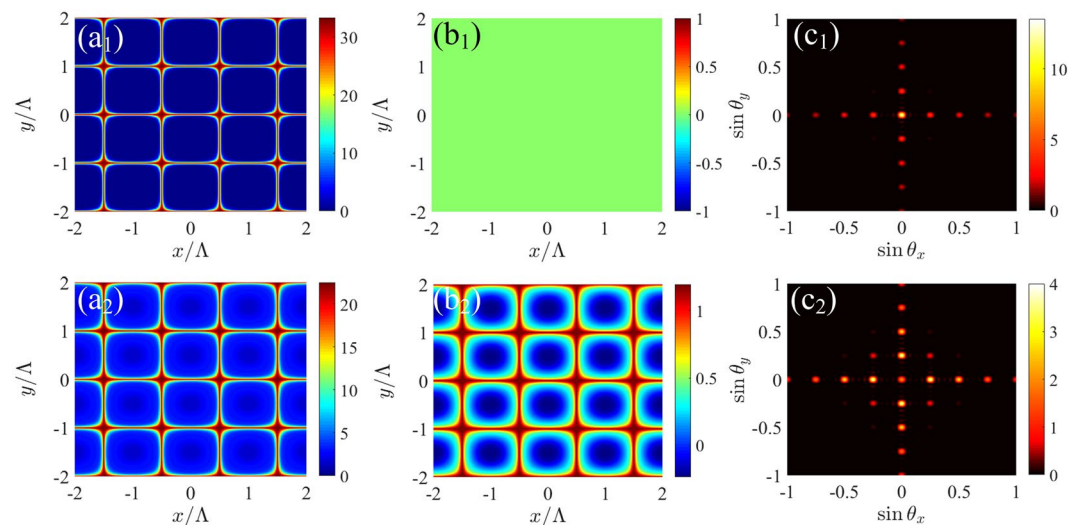


Figure 6. (a₁, a₂) The amplitude $|T(x, y)|$ and (b₁, b₂) the phase $\Phi(x, y)/\pi$ of 2D transmission function as a function of (x, y) , and (c₁, c₂) Fraunhofer diffraction intensity $I_p(\theta_x, \theta_y)$ as a function of $(\sin \theta_x, \sin \theta_y)$ for different R and Δ_p . (a₁, b₁, c₁) $R = 1.833\Gamma$ and $\Delta_p = 0$; (a₂, b₂, c₂) $R = 3.91\Gamma$ and $\Delta_p = 12\Gamma$. Other parameters are $\Omega_{d0} = 8\Gamma$, $\Delta_d = 0$, $M_x = M_y = 5$, $\Lambda/\lambda_p = 4$ and $L = 180\zeta$.

that the most portion of probe energy is diffracted into the $(\pm m, 0)$ - and $(0, \pm n)$ -order diffraction directions and the $(0, 0)$ -order diffraction field dominates [see Fig. 6(c₁)]. Here, the diffraction intensity in the first diffraction order, i.e., $(\pm 1, 0)$ and $(0, \pm 1)$ orders, can arrive at 4. When $R = 3.91\Gamma$ and $\Delta_p = 12\Gamma$, as shown in Fig. 6(a₂, b₂), the maxima of the phase $\Phi(x, y)$ are localized at the positions, where the amplitude $|T(x, y)|$ is maximal. Although the amplitude $|T(x, y)|$ of the transmission function reduces in comparison with the case shown in Fig. 6(a₁), but the approximate π phase modulation depth results in more probe energy being diffracted into the high-order diffraction directions. In this case, the diffraction intensities of the $(\pm 1, 0)$ - and $(0, \pm 1)$ -order diffraction fields can also reach 4 [see Fig. 6(c₂)]. To see more details, the evolutions of the diffraction intensities in the $(0, 0)$, $(0, 1)$, $(0, 2)$ and $(1, 1)$ diffraction orders with the incoherent pumping rate R and probe detuning Δ_p are plotted in Fig. 7. Similar to the 1D case, the studied four diffraction fields increase monotonically as R increases or Δ_p decreases and the $(0, 1)$ - and $(0, 2)$ -order diffraction intensities exceed the $(0, 0)$ -order diffraction intensity for large R or Δ_p [see Fig. 7(a, b)]. Therefore, it can be concluded that the location of the maximal diffraction field of 2D grating can be manipulated via adjusting the values of R and Δ_p .

We further examine in Fig. 8 the influence of the 2D space-dependent driving field on the diffraction of 2D grating. The evolutions of the diffraction intensities in the $(0, 0)$, $(0, 1)$, $(0, 2)$ and $(1, 1)$ diffraction orders with the intensity Ω_{d0} and the detuning Δ_d of the driving field are plotted in Fig. 8(a, b), respectively. It is found that increasing Ω_{d0} or decreasing Δ_d can lead to the reduction of the $(0, 0)$ -order diffraction intensity but the diffraction intensities in the $(0, 1)$ and $(0, 2)$ diffraction orders increase firstly and then decrease. These trends are similar to the 1D cases shown in Fig. 4(a, b). However, unlike the $(0, 1)$ - and $(0, 2)$ -order diffraction fields, the $(1, 1)$ -order diffraction field shows fluctuation in the diffraction intensity with respect to Ω_{d0} and Δ_d .

Finally, we examine in Fig. 9 what will happen when the same system parameters are selected for both 1D and 2D gratings? Here, we select the same parameters in Fig. 2(c₂) except $R = 3.32\Gamma$ and $M = M_x = M_y = 5$. One can find from Fig. 9(a, b) that the first-order diffraction field dominates in the diffraction of 1D grating, while the $(0, 0)$ -order diffraction field is maximal in the diffraction of 2D grating. Meanwhile, the first-order diffraction

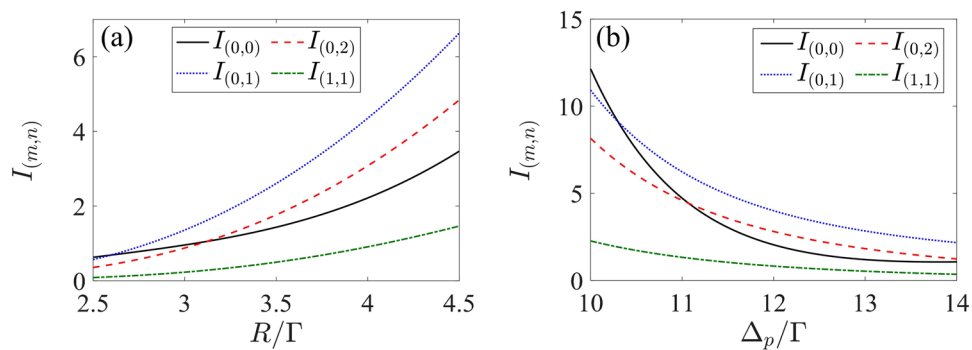


Figure 7. Fraunhofer diffraction intensities of 2D grating for some diffraction orders as a function of (a) the incoherent pumping rate R with $\Delta_p = 12\Gamma$ and (b) the probe detuning Δ_p with $R = 3.91\Gamma$. Other parameters are the same as in Fig. 6.

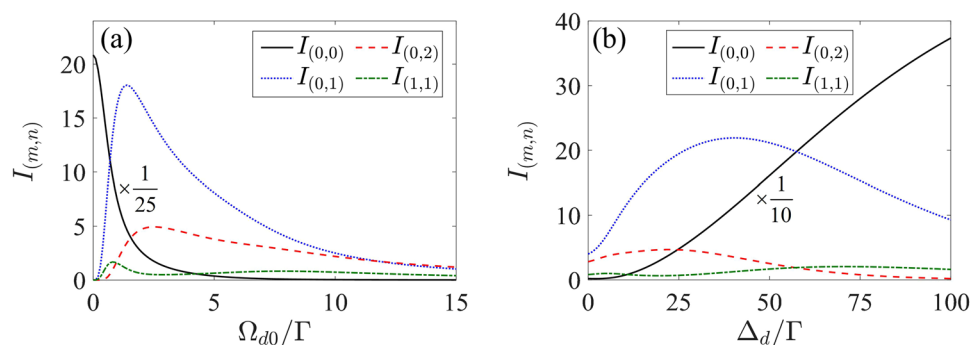


Figure 8. Fraunhofer diffraction intensities of 2D grating for some diffraction orders as a function of (a) the intensity Ω_{d0} with $\Delta_d = 0$ and (b) the detuning Δ_d with $\Omega_{d0} = 8\Gamma$ of the SW driving field. Other parameters are the same as in Fig. 6 except for $R = 3.91\Gamma$ and $\Delta_p = 12\Gamma$.

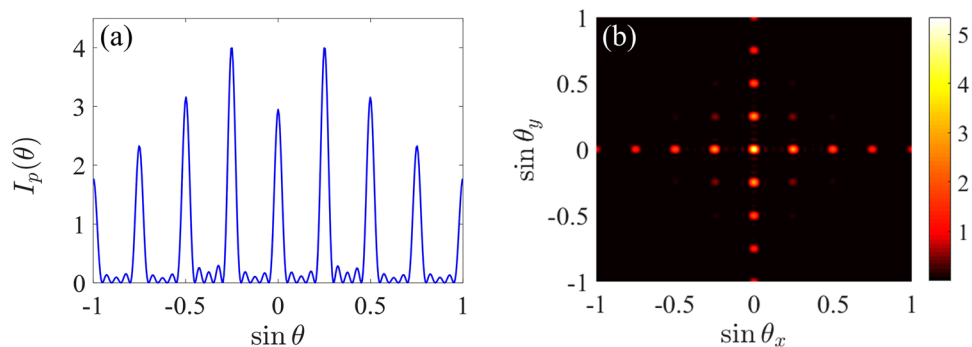


Figure 9. Fraunhofer diffraction spectra of (a) 1D and (b) 2D gratings for $R = 3.32\Gamma$ and $M = M_x = M_y = 5$. Other parameters are the same as in Fig. 2(c₂).

intensity, i.e., $I_1 = 4$, is larger than the (0, 1)-order diffraction intensity, i.e., $I_{(0,1)} = 3.32$. These results indicate that 1D and 2D EIGs exhibit different diffraction characteristics for the same optical parameters.

In summary, we have theoretically investigated the Fraunhofer diffraction of 1D and 2D EIGs realized in Er^{3+} -doped YAG crystal. In the presence of the incoherent pumping process, the induced spatial gain modulation without or with phase modulation results in the generation of the gain or hybrid grating, where the high diffraction intensities are achievable in the high-order diffraction directions. It is demonstrated that increasing the incoherent pumping rate and decreasing the probe detuning can significantly improve the diffraction efficiencies of the 1D and 2D crystal gratings. We give a suitable physical interpretation for the diffraction behaviors via the interference of the gain and phase gratings. Furthermore, it is found that the diffraction intensity of each diffraction field is also controllable by tuning the intensity and detuning of the SW driving field or the concentration of Er^{3+} ion. More importantly, the probe energy of the diffraction side lobes around the central principal maximum

is comparable to that of the first-order diffraction field for small driving intensity or large driving detuning, which would limit the use of the first-order diffraction component. Based on this situation, we find the suitable optical parameters to realize the optimal performance of the grating. Finally, we note that the transition ${}^4I_{15/2} \rightarrow {}^4I_{13/2}$ driven by weak probe field coincides with the third transparency-window of the optical fiber. Therefore, our scheme may provide the possibility for the active all-optical control of optical switching, routing and storage in communication wavelengths.

Received: 12 September 2019; Accepted: 18 February 2020;

Published online: 04 March 2020

References

- Brown, A. W. & Xiao, M. All-optical switching and routing based on an electromagnetically induced absorption grating. *Opt. Lett.* **30**, 699–701 (2005).
- Chen, Y. Y., Liu, Z. Z. & Wan, R. G. Beam splitter and router via an incoherent pump-assisted electromagnetically induced blazed grating. *Appl. Opt.* **56**, 5736–5744 (2017).
- Zhai, P. W., Su, X. M. & Gao, J. Y. Optical bistability in electromagnetically induced grating. *Phys. Lett. A* **289**, 27–33 (2001).
- Tabosa, J. & Lezama, A. Light grating storage in cold atoms. *J. Phys. B: At. Mol. Opt. Phys.* **40**, 2809–2815 (2007).
- Wen, J., Du, S., Chen, H. & Xiao, M. Electromagnetically induced talbot effect. *Appl. Phys. Lett.* **98**, 081108 (2011).
- Qiu, T. Electromagnetically induced holographic imaging in hybrid artificial molecule. *Opt. Express* **23**, 24537–24546 (2015).
- Zhang, Y. *et al.* Four-wave mixing dipole soliton in laser-induced atomic gratings. *Phys. review letters* **106**, 093904 (2011).
- Ling, H. Y., Li, Y.-Q. & Xiao, M. Electromagnetically induced grating: Homogeneously broadened medium. *Phys. Rev. A* **57**, 1338–1344 (1998).
- Mitsunaga, M. & Imoto, N. Observation of an electromagnetically induced grating in cold sodium atoms. *Phys. Rev. A* **59**, 4773–4776 (1999).
- Cardoso, G. & Tabosa, J. Electromagnetically induced gratings in a degenerate open two-level system. *Phys. Rev. A* **65**, 033803 (2002).
- de Araujo, L. E. E. Electromagnetically induced phase grating. *Opt. Lett.* **35**, 977–979 (2010).
- Xiao, Z. H., Shin, S. G. & Kim, K. An electromagnetically induced grating by microwave modulation. *J. Phys. B: At. Mol. Opt. Phys.* **43**, 161004 (2010).
- Carvalho, S. A. & de Araujo, L. E. Electromagnetically induced blazed grating at low light levels. *Phys. Rev. A* **83**, 053825 (2011).
- Kuang, S. Q., Jin, C. S. & Li, C. Gain-phase grating based on spatial modulation of active Raman gain in cold atoms. *Phys. Rev. A* **84**, 033831 (2011).
- Wan, R. G., Kou, J., Jiang, L., Jiang, Y. & Gao, J. Y. Electromagnetically induced grating via enhanced nonlinear modulation by spontaneously generated coherence. *Phys. Rev. A* **83**, 033824 (2011).
- Wang, L., Zhou, F., Hu, P., Niu, Y. & Gong, S. Two-dimensional electromagnetically induced cross-grating in a four-level tripod-type atomic system. *J. Phys. B: At. Mol. Opt. Phys.* **47**, 225501 (2014).
- Zhao, L. Electromagnetically induced polarization grating. *Sci. reports* **8**, 3073 (2018).
- Liu, Y. M., Gao, F., Fan, C. H. & Wu, J. H. Asymmetric light diffraction of an atomic grating with \mathcal{PT} symmetry. *Opt. Lett.* **42**, 4283–4286 (2017).
- Shui, T., Yang, W. X., Liu, S. P., Li, L. & Zhu, Z. H. Asymmetric diffraction by atomic gratings with optical \mathcal{PT} symmetry in the Raman-Nath regime. *Phys. Rev. A* **97**, 033819 (2018).
- Shui, T., Yang, W. X., Li, L. & Wang, X. Lop-sided Raman-Nath diffraction in \mathcal{PT} -antisymmetric atomic lattices. *Opt. Lett.* **44**, 2089–2092 (2019).
- Asghar, S., Ziauddin, Qamar, S. & Qamar, S. Electromagnetically induced grating with Rydberg atoms. *Phys. Rev. A* **94**, 033823 (2016).
- Ma, D., Yu, D., Zhao, X.-D. & Qian, J. Unidirectional and controllable higher-order diffraction by a Rydberg electromagnetically induced grating. *Phys. Rev. A* **99**, 033826 (2019).
- Liu, J. *et al.* Electromagnetically induced grating in a crystal of molecular magnets system. *Phys. Lett. A* **380**, 2458–2464 (2016).
- Zhou, F. *et al.* Electromagnetically induced grating in asymmetric quantum wells via Fano interference. *Opt. Express* **21**, 12249–12259 (2013).
- Cheng, G. L., Zhong, W. X. & Chen, A. X. Phonon induced phase grating in quantum dot system. *Opt. Express* **23**, 9870–9880 (2015).
- Tian, S. C. *et al.* Asymmetric light diffraction of two-dimensional electromagnetically induced grating with PT symmetry in asymmetric double quantum wells. *Opt. Express* **26**, 32918–32930 (2018).
- Bozorgzadeh, F. & Sahrhai, M. Laser-induced diffraction grating in asymmetric double quantum well nanostructure. *Laser Phys. Lett.* **16**, 036002 (2019).
- Xiao, Z. H., Zheng, L. & Lin, H. Z. Photoinduced diffraction grating in hybrid artificial molecule. *Opt. Express* **20**, 1219–1229 (2012).
- You, Y., Qi, Y. H., Niu, Y. P. & Gong, S. Q. Control of electromagnetically induced grating by surface plasmon and tunneling in a hybrid quantum dot-metal nanoparticle system. *J. Physics: Condens. Matter* **31**, 105801 (2019).
- Zharikov, E. V. *et al.* Stimulated emission from Er^{3+} ions in yttrium aluminum garnet crystals at $\lambda = 2.94 \mu$. *Sov. J. Quantum Electron.* **4**, 1039–1040 (1975).
- Svelto, O. & Hanna, D. C. *Principles of lasers*, vol. 4 (Springer, 1998).
- Xu, H., Dai, Z. & Jiang, Z. Effect of concentration of the Er^{3+} ion on electromagnetically induced transparency in Er^{3+} : YAG crystal. *Phys. Lett. A* **294**, 19–25 (2002).
- Zhang, H.-F., Wu, J.-H., Su, X.-M. & Gao, J.-Y. Quantum-interference effects on the index of refraction in an Er^{3+} -doped yttrium aluminum garnet crystal. *Phys. Rev. A* **66**, 053816 (2002).
- Qian, J., Zhang, H. F. & Gao, J. Y. Positive and negative dispersion in an Er^{3+} -doped yttrium aluminum garnet crystal. *JOSAB* **21**, 1364–1368 (2004).
- Wang, G., Yan, X., Wu, J. H. & Gao, J. Y. The phase dependent properties of gain and absorption in an Er^{3+} -doped yttrium aluminum garnet crystal. *Opt. Commun.* **267**, 118–123 (2006).
- Wang, Z. Optical bistability via coherent and incoherent fields in an Er^{3+} -doped yttrium-aluminum-garnet crystal. *Opt. Commun.* **283**, 3291–3295 (2010).
- Asadpour, S. H. & Soleimani, H. R. Comparison of optical properties between ladder and lambda-type EIT medium with Er^{3+} ion concentration in Er^{3+} : Yag crystal. *J. Mater. Sci. Mater. Electron.* **25**, 3578–3585 (2014).
- Judd, B. R. Optical absorption intensities of rare-earth ions. *Phys. Rev.* **127**, 750 (1962).
- Ofeld, G. Intensities of crystal spectra of rare-earth ions. *J. Chem. Phys.* **37**, 511–520 (1962).
- Kaminskii, A. *et al.* New laser properties and spectroscopy of orthorhombic crystals $\text{YAlO}_3: \text{Er}^{3+}$. *Physica Status Solidi A* **151**, 231–255 (1995).
- Wang, Q., Zhang, S. & Jia, Y. Effect of the concentration of the Er^{3+} ion on the spectral intensity parameters of Er^{3+} : Yag crystals. *J. Alloy. Compd.* **202**, 1–5 (1993).

42. Zhekov, V. *et al.* Cooperative process in $\text{Y}_3\text{Al}_5\text{O}_{12}:\text{Er}^{3+}$ crystals. *Sov. J. Quantum Electron.* **16**, 274–276 (1986).
43. Sun, Y., Thiel, C., Cone, R., Equall, R. & Hutcheson, R. Recent progress in developing new rare earth materials for hole burning and coherent transient applications. *J. Lumin.* **98**, 281–287 (2002).
44. Pokhrel, M. *et al.* Infrared and upconversion spectroscopic studies of high Er^{3+} content transparent YAG ceramic. *Opt. Mater. Express* **1**, 1272–1285 (2011).
45. Yin, J. *et al.* Gain and noise figure analysis of Er^{3+} -doped YAG transparent ceramic microchip amplifier. *J. Shanghai Jiaotong Univ.* **22**, 406–410 (2017).

Acknowledgements

This work is supported in part by National Natural Science Foundation of China (11374050 and 11774054).

Author contributions

T.S. performed the theoretical analysis and wrote the main manuscript. W.-X.Y. conceived the idea, supervised T.S. and checked the numerical simulations. L.L. and X.W. discussed and checked the computational results.

Competing interests

The authors declare no competing interests.

Additional information

Correspondence and requests for materials should be addressed to W.-X.Y.

Reprints and permissions information is available at www.nature.com/reprints.

Publisher's note Springer Nature remains neutral with regard to jurisdictional claims in published maps and institutional affiliations.



Open Access This article is licensed under a Creative Commons Attribution 4.0 International License, which permits use, sharing, adaptation, distribution and reproduction in any medium or format, as long as you give appropriate credit to the original author(s) and the source, provide a link to the Creative Commons license, and indicate if changes were made. The images or other third party material in this article are included in the article's Creative Commons license, unless indicated otherwise in a credit line to the material. If material is not included in the article's Creative Commons license and your intended use is not permitted by statutory regulation or exceeds the permitted use, you will need to obtain permission directly from the copyright holder. To view a copy of this license, visit <http://creativecommons.org/licenses/by/4.0/>.

© The Author(s) 2020